Earth and Planetary Science Letters 528 (2019) 115832

Contents lists available at ScienceDirect

Earth and Planetary Science Letters

www.elsevier.com/locate/epsl

Experimental evidence for wall-rock pulverization during dynamic rupture at ultra-high pressure conditions

Sarah Incel [a,*], Alexandre Schubnel [b], Jörg Renner [c], Timm John [d], Loïc Labrousse [e], Nadège Hilairet [f], Helen Freeman [g], Yanbin Wang [h], François Renard [a,i], Bjørn Jamtveit [a]

[a] Physics of Geological Processes, The Njord Centre, Department of Geosciences, University of Oslo, Box 1048 Blindern, 0316 Oslo, Norway
[b] Laboratoire de Géologie de l'ENS - PSL Research University - UMR8538 du CNRS, 24 Rue Lhomond, 75005 Paris, France
[c] Ruhr-Universität Bochum, Universitätsstraße 150, 44801 Bochum, Germany
[d] Freie Universität Berlin, Institute of Geological Sciences, Malteserstr. 74-100, 12249 Berlin, Germany
[e] Sorbonne Université, CNRS-INSU, Institut des Sciences de la Terre Paris, ISTeP, UMR 7193, 75005 Paris, France
[f] Univ. Lille, CNRS, INRA, ENSCL, UMR 8207 - Unité Matériaux et Transformations, 59000 Lille, France
[g] Helmholtz-Zentrum Potsdam, Deutsches GeoForschungsZentrum GFZ, Telegrafenberg, 14473 Potsdam, Germany
[h] Center for Advanced Radiation Sources, the University of Chicago, Chicago, IL 60637, USA
[i] Univ. Grenoble Alpes, Univ. Savoie Mont Blanc, CNRS, IRD, IFSTTAR, ISTerre, 38000 Grenoble, France

ARTICLE INFO

Article history:
Received 25 March 2019
Received in revised form 30 August 2019
Accepted 9 September 2019
Available online xxxx
Editor: J. Brodholt

Keywords:
pulverization
high-pressure deformation
dynamic rupture
lawsonite-blueschist
DDIA apparatus
acoustic emissions

ABSTRACT

The mechanisms triggering intermediate and deep earthquakes have puzzled geologists for several decades. There is still no consensus concerning whether such earthquakes are triggered by brittle or ductile mechanisms. We performed a deformation experiment on a synthetic lawsonite-bearing blueschist at a confining pressure of 3 GPa and temperatures from 583 to 1,073 K. After deformation, the recovered sample reveals conjugated shear fractures. Garnet crystals are dissected and displaced along these narrow faults and reveal micro- and nanostructures that resemble natural pulverization structures as well as partial amorphization. Formation of such structures at low confining pressures is known to require high tensile stresses and strain rates and is explained by the propagation of a dynamic shear rupture. The absence of shearing in the pulverized wall rock is taken as evidence that these structures pre-date the subsequent heat-producing frictional slip. In analogy to observations at low pressure we infer that the garnet structures in our experiment result from rapid propagation of a shear fracture even at the high pressure exerted on the sample and thus suggest that brittle deformation is possible at lower crustal to upper mantle depths.

1. Introduction

During subduction at convergent plate margins, intermediate depth (70-300 km) and deep (>300 km) earthquakes are common. Yet, the processes triggering earthquakes at the high pressures (>1 GPa) prevailing at these depths are poorly understood. Both brittle (Raleigh and Paterson, 1965; Kirby, 1987; Green II and Burnley, 1989; Schubnel et al., 2013; Okazaki and Hirth, 2016; Ferrand et al., 2017; Gasc et al., 2017; Incel et al., 2019, 2017; and references therein) and ductile (Braeck and Podladchikov, 2007; Kelemen and Hirth, 2007; John et al., 2009; Thielmann et al., 2015; and references therein) mechanisms have been proposed.

While the suggested ductile mechanisms involve self-localizing failure by dissipative heating and thermal runaway situations, the considered brittle mechanisms involve dynamic rupture. In the former case, one expects significant shear deformation prior to seismic slip, whereas in the latter case, wall-rock damage may occur due to high tensile stresses and strain rates near a propagating rupture tip prior to frictional heating of the shear fracture surfaces (Ben-Zion, 2003; Xu and Ben-Zion, 2017; Griffith et al., 2018). Wall-rock deformation associated with paleo-earthquakes inferred from the presence of pseudotachylytes, a rock type often assumed to be the result of frictional melting and subsequent quenching (McKenzie and Brune, 1972; Sibson, 1975), was interpreted as evidence for a thermal runaway mechanism (John et al., 2009). Studies of pseudotachylyte veins and their surrounding wall rocks in naturally deformed rocks do, however, pose a number of challenges due to postseismic deformation and recovery processes with respect to their formation (Guermani and Pennacchioni, 1998; Mancktelow, 2006; Kirkpatrick and Rowe, 2013). Recent microstructural observations indicate extremely high stresses in wall rocks

* Corresponding author.
E-mail address: s.h.m.incel@geo.uio.no (S. Incel).

https://doi.org/10.1016/j.epsl.2019.115832
0012-821X/

around lower crustal earthquake zones, and abundant fragmentation (Angiboust et al., 2012) without observable shear (Austrheim et al., 2017; Petley-Ragan et al., 2018, 2019; Jamtveit et al., 2019). Such fragmentation is often referred to as 'pulverization' when occurring around faults in the shallow seismogenic regime and is assumed to result from dynamic rupture processes (Dor et al., 2006; Mitchell and Faulkner, 2009; Rempe et al., 2013).

In a previous experimental study, synthetic polycrystalline lawsonite-bearing blueschist samples were deformed at confining pressures corresponding to upper mantle depths (Incel et al., 2017). Faulting was accompanied by the record of acoustic emissions and the growth of eclogite-facies minerals monitored using in-situ powder diffraction. Examination of the recovered run products revealed several conjugated faults decorated with nanocrystalline eclogite-facies transformation products in samples that entered the stability field of eclogite. Therefore, Incel et al. (2017) suggested that failure occurred due to transformation-induced instabilities, a mechanism titled transformational faulting (see also Kirby, 1987; Green II and Burnley, 1989). In one of these samples (BS_3_1073 in Incel et al., 2017), garnet grains that are cut and displaced by the faults show microstructures similar to what has been described from 'pulverized' garnets in natural fault rocks from lower crustal lithologies (Austrheim et al., 2017; Petley-Ragan et al., 2018, 2019; Jamtveit et al., 2019). Here, we further investigate the micro- and nanostructure of different garnets found in this sample. In addition, we model the spatial relation of the occurrence and absence of garnet fracturing relying on linear elastic fracture mechanics with the aim to gain further insight into the dynamics of intermediate-depth earthquakes.

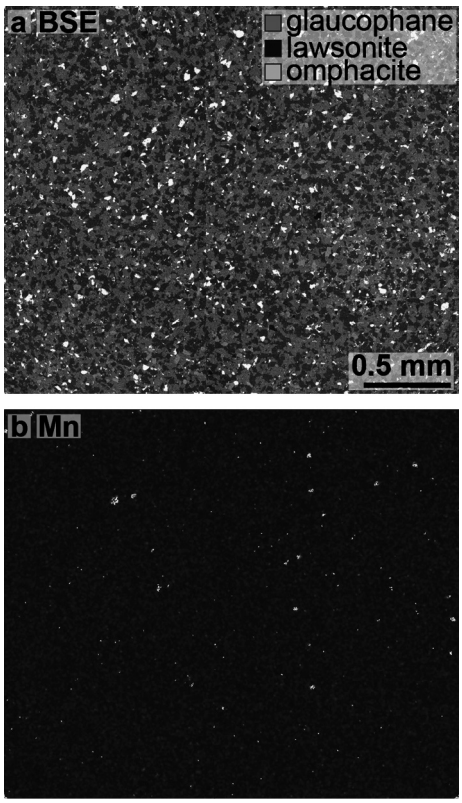

Fig. 1. The starting material after hot-pressing. a) Backscattered electron (BSE) image showing that the phases are homogeneously distributed throughout the sample. b) A Mn-distribution map of the same region was used to highlight the location of garnet crystals.

2. Experimental methods and analytical techniques

2.1. Sample description and preparation of the starting material

A lawsonite-bearing blueschist from Alpine Corsica served as sample material. To avoid any initial texture of the starting material a chemically homogeneous part of this blueschist was crushed and sieved to a grain size <38 µm. The major phases are glaucophane and lawsonite in a ratio of $\sim$3:2 making up $\sim$90 vol.% of the powder. Minor and accessory phases are garnet, omphacite, actinolite, titanite, and phengite. The blueschist powder was hot-pressed at 3 GPa and 923 K for 24 h in a piston-cylinder and machined to approx. 2.1 mm in diameter and 3 mm in height. After hot-pressing, the sample's phases reveal a homogeneous texture (Fig. 1a). In particular, the garnets are randomly distributed throughout the sample as evidenced by the Mn-element distribution map (Fig. 1b).

2.2. D-DIA deformation experiment

A $9 \times 9 \times 8$ mm sized amorphous Boron-epoxy cuboid was used as pressure medium for the experiment performed using a D-DIA apparatus. The hot-pressed sample is located in the middle of this cuboid, sandwiched between two gold foils and two alumina pistons, and surrounded by a hexagonal Boron Nitride (hBN) sleeve that is inserted into a graphite furnace. The deformation apparatus is mounted on the GSECARS beamline at the Advanced Photon Source, National Laboratory, Argonne, IL, USA. The use of synchrotron radiation during deformation made it possible to calculate the differential stress as well as the strain and the strain rate during deformation. Using powder diffraction patterns, stress of the deforming sample was calculated based on the change in lattice spacing of glaucophane. For each diffraction the incident monochromatic beam was collimated to 200 µm $\times$ 200 µm by tungsten carbide slits. Therefore, diffraction patterns were taken of a small volume in the central part of the sample. Strain was measured by using radiographs of the entire sample. Either measurement was performed every five minutes during deformation resulting in a time resolution for stress and strain of approx. 300 s. Details of the stress and strain calculation are described by Incel et al. (2017).

The D-DIA apparatus is equipped with an acoustic emission (AE) system comprising six transducers placed behind the deformation anvils. Acoustic signals were amplified at 60 dB, monitored in trigger mode with a trigger threshold of 250 mV on two channels. Upon triggering, individual AEs were recorded using a sampling rate of 50 MHz. The duration of the largest AEs recorded was in the range of a few hundreds of microseconds. Hence, the time resolution of the stress measurements is around six magnitudes poorer than the event duration. Further details on the experimental setup can be found in Wang et al. (2003), Gasc et al. (2011), or Schubnel et al. (2013).

The sample was first loaded hydrostatically to a confining pressure (P_c) of approx. 3 GPa (here confining pressure P_c equals the least principal stress σ_3) and then heated to a temperature of approx. 583 K by manually increasing the electric power going through the graphite furnace (Joule heating). The sample was kept at these conditions for 30 min before deformation with a strain rate of approx. 5×10^{-5} s^{-1} commenced. While deformation of the sample proceeded, electric power was increased in 10 W steps to heat up the sample from initially 583 to 1073 K. Heating steps were initiated at 5, 12, 18, 20, 25, 30, and 35 % axial strain.

2.3. Analytical techniques

Microstructural analyses of the recovered sample were performed using a field-emission scanning electron microscope (FE-

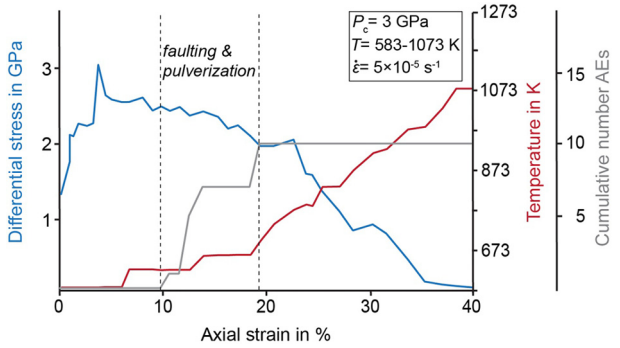

Fig. 2. Differential stress, temperature, and cumulative number of acoustic emission (AE) events over axial strain. Based on the record of AEs (grey curve), faulting and pulverization occurs at a confining pressure (P_c) = 3 GPa, a differential stress of ~2.5 GPa (blue curve), in a temperature range of 640 to 720 K (red curve), at an imposed strain rate ($\dot{\varepsilon}$) = 5 × 10^{-5} s^{-1}, and an axial strain ε = ~10–19 %. (For interpretation of the colors in the figure(s), the reader is referred to the web version of this article.)

SEM) with an acceleration voltage of 15 kV. To investigate the nanostructure of this sample, three focused-ion beam (FIB) sections were cut using a FEI-Helios G4 UC-Dual Beam system for imaging, analysis and transmission electron microscopy (TEM). The nanostructural analyses were conducted using a FEI Tecnai TEM and a Jeol JEM 2011 transmission electron microscope. For both machines, the acceleration voltage was 200 keV.

3. Results

3.1. Mechanical data and acoustic emissions

During the first stage of deformation at a temperature of 583 K, the sample was strained by 5 % and the differential stress increased to a peak stress of approx. 3 GPa, i.e. the level of the confining pressure or Goetze criterion (Fig. 2). The differential stress then decreased continuously during syndeformational heating of the sample. A total axial strain of 40 % was accumulated by the time the temperature reached 1073 K. In total, 10 AEs were recorded between 10 to 19 % axial strain. Two events, recorded at around 12 % and 19 % axial strain, were events large enough that they almost reached voltage saturation of the recording system (5 V).

3.2. Microstructural analyses

Microstructural investigations using the field-emission scanning electron microscope (FE-SEM) revealed faults, oriented at an angle of around 45° to the direction of the axial stress σ_1, crosscutting the entire sample (Fig. 3a). It is possible that either some of the fault-filling material (gouge) of the major faults was lost during sample preparation or the fault surfaces were separated during decompression. However, some relicts of gouge material are preserved at the fault borders. These relicts show holes after interaction with the electron beam of the SEM, implying that this material is poorly crystalline (Fig. 3c).

Two different types of garnets can be identified in the deformed sample, (i) garnet crystals that are dissected and displaced along narrow faults (<1 µm wide; Figs. 3c; 4a–c) and (ii) unsheared garnet grains situated at some distance to the nearest fault (~0.5 to 1.5 mm; Figs. 3b, 4d, e). Two example sets of displaced garnet parts show apparent shear displacements of 42 and 58 µm (Figs. 3c; 4a). Back-scattered electron (BSE) imaging reveals that the displaced garnet halves are fragmented into pieces with diameters <1 µm (Figs. 3d; 4b), some of which were dragged into the principal slip plane (red arrow in Fig. 3d). Garnet grains located further away from the fractures do not exhibit fragmentation at this magnification in the SEM (Figs. 3b; 4d, e).

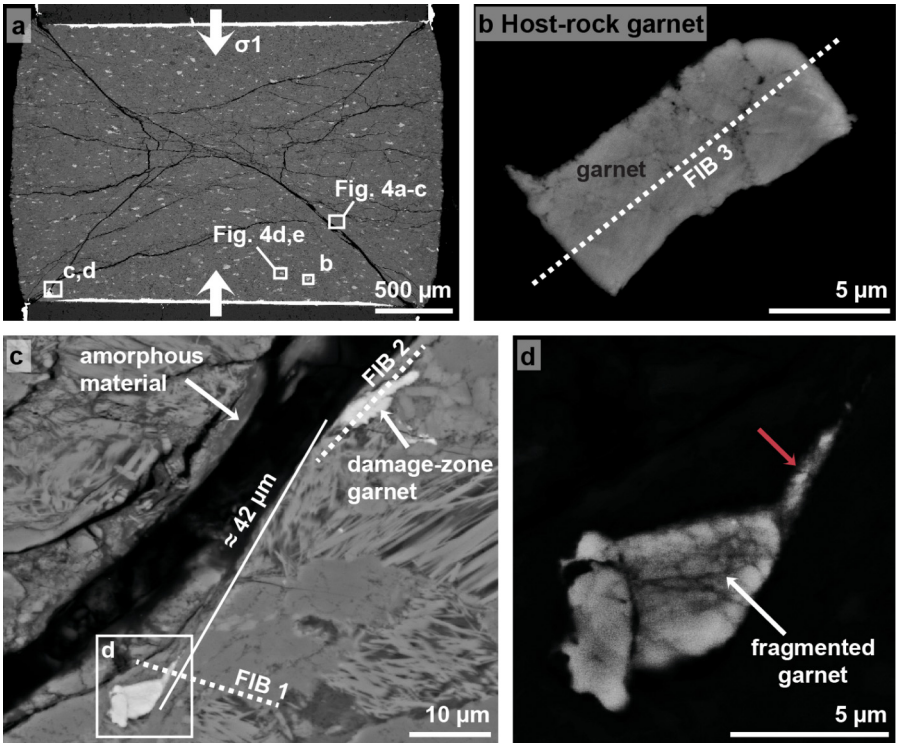

Fig. 3. Backscattered electron images of the lawsonite-bearing blueschist sample after deformation. a) Overview image of the sample showing faults oriented at ~45° towards σ_1 crosscutting the sample. The positions of the high-magnification images in b–d as well as the position for Fig. 4 are highlighted with white rectangles, respectively. b) The host-rock garnet crystal that is located at ~0.5 µm to the closest fault. The location of FIB section 3 is shown as white dashed line. c) A garnet pair that is dissected and displaced along a narrow fault. The apparent displacement is ~42 µm. The locations for FIB sections 1 and 2 are marked by white dashed lines. The white rectangle shows the location of a garnet half presented in d. d) At high magnification and high brightness contrast the garnet half appears fragmented into several pieces <1 µm.

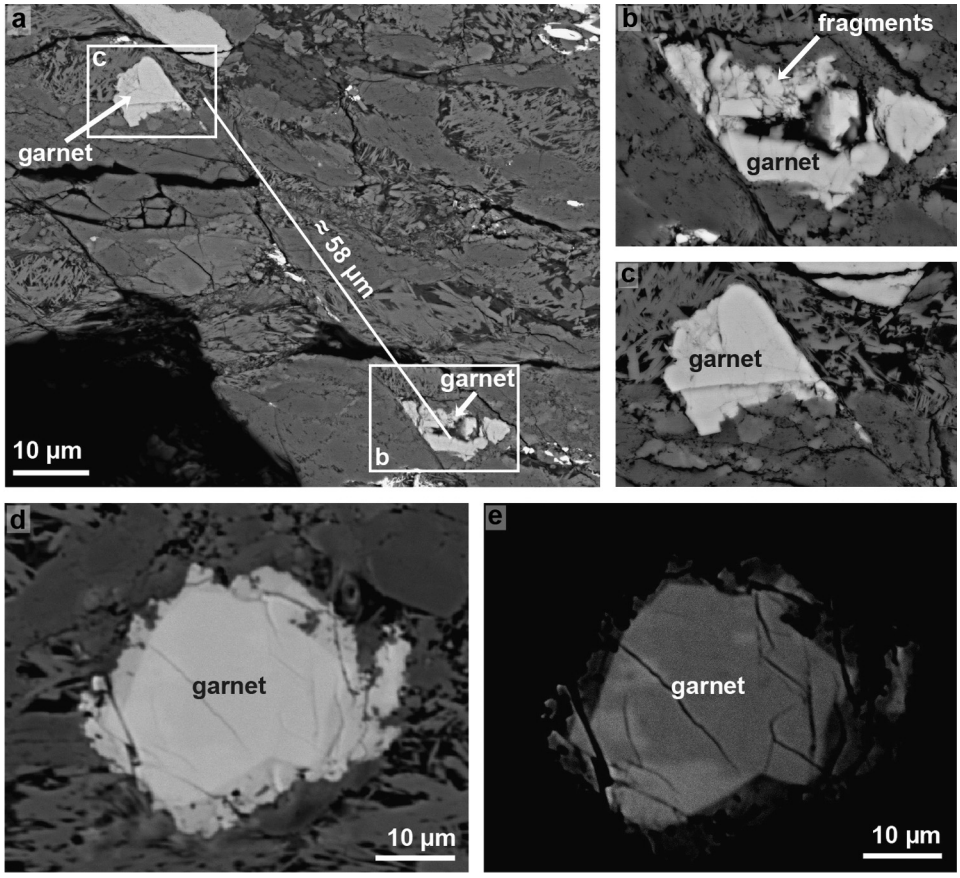

Fig. 4. a) Backscattered electron images of another pair of dissected and displaced crystals that are offset by a narrow fault. The offset along the narrow fault is ~58 µm. b and c) The two halves of the garnet pair showing extensive fragmentation in b). d and e) This garnet was found at ~1 mm from the nearest fault and seems relatively intact. e) Same crystal as in d) with the image taken at a higher brightness contrast at the SEM.

3.3. Nanostructural analyses

Transmission electron microscope (TEM) analyses were performed at three different sites (Fig. 3b, c) to investigate the nanometer-scale structures of: (i) the fault-gouge of the narrow fault dissecting and displacing a garnet crystal, (ii) a garnet crystal that is cut by this narrow fault, hereafter referred to as damage-zone garnet, and (iii) a garnet crystal located at a minimum of ~0.5 mm from any fault, denoted as host-rock garnet. The fault-gouge contains garnet crystals with sizes ranging from <20 nm to ~100 nm. In bright field mode TEM images, the material embedding the garnets appeared brighter than the garnet grains (Fig. 5a). An electron diffraction pattern of this area showed a few diffraction spots but also a diffuse halo (Fig. 5b) implying a combination of domains that have lost their long-range crystalline order and crystals large enough to produce diffraction spots.

Scanning transmission electron microscopy (STEM) of the damage-zone garnet demonstrates that this grain is completely shattered into small fragments that range in size from ~10 nm to ~1 µm (Figs. 5c, 6a) and are surrounded by a fault-filling material exhibiting vesicles and idiomorphic crystals (Fig. 6a). Using energy-dispersive spectroscopy (EDS) measurements these idiomorphic crystals were identified as omphacite. The surrounding matrix mainly consists of Si, Al, Na, and Ca in addition to O. The diffraction pattern obtained from a circular area with a diameter of ~500 nm in the shattered damage-zone garnet shows few large and several weak diffraction spots, indicative of a polycrystalline material, together with a diffuse halo in its center (Fig. 5c, d). This halo is less prominent than the one obtained from diffraction of the fault-gouge (Fig. 5b). A bright-field and a dark-field-mode image of the same area within the shattered damage-zone garnet that were taken at high magnification document grain-size and crystal-orientation variation, respectively (Fig. 6b, c). The bright-field image shows several grains ranging in size from ~10 to ~50 nm in diameter (Fig. 6b). A quantitative determination of the grain-size distribution is hampered by the abundant overlap of small grains. Lattice fringes are clearly visible locally (Fig. 6c). However, the brightness variation in the corresponding dark-field-mode image suggests variations in lattice orientation on the nanometer scale.

In contrast to the nanostructure of the damage-zone garnet revealing numerous fragments of only a few tens of nanometer, the nanostructural analysis of the host-rock garnet mainly shows features that resemble subgrains ranging in diameter from several hundred nanometers to ~2 µm (Fig. 5e). A diffraction pattern of an area with a diameter of ~500 nm (Fig. 5e) indicates a high degree of crystallinity in this zone (Fig. 5f).

4. Discussion

4.1. Garnet pulverization due to dynamic rupture propagation

Our microscopic analyses revealed extensive fragmentation of the damage-zone garnet. Its diffraction pattern shows numerous weak diffraction spots indicating the presence of many small crystals. Additionally, a diffuse halo is observed implying that some subdomains are either amorphous or too small (<10 nm) to produce well-defined diffraction spots (Fig. 6c; Yund et al., 1990). On the contrary, the host-rock garnet is fully crystalline revealing the

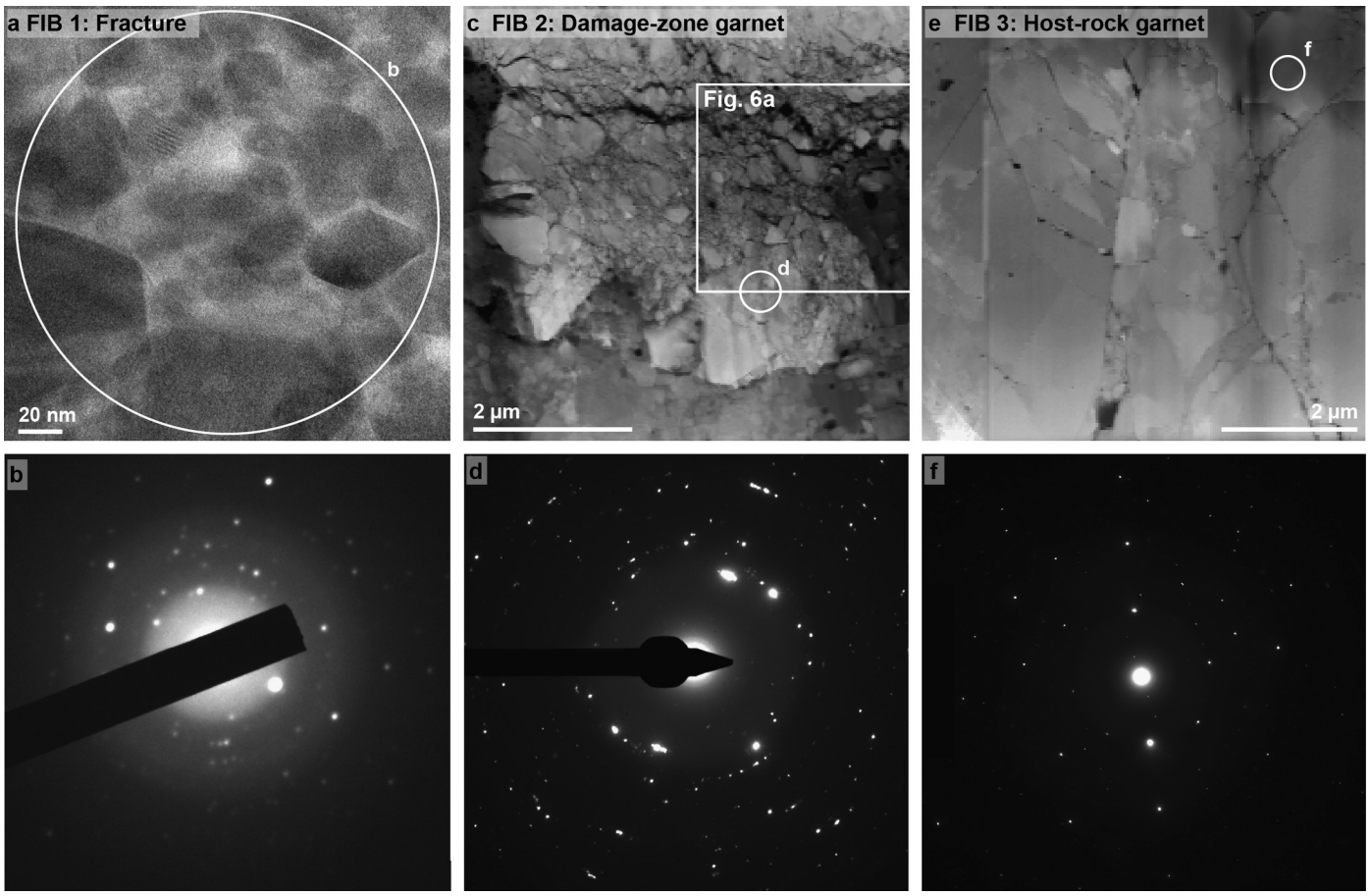

Fig. 5. Transmission electron microscope images of the three FIB sections 1–3. a and b) FIB 1 revealing the fault-filling material. a) Bright field image showing dark (i.e. crystalline) garnet crystals floating in a bright (i.e. amorphous) material. The location chosen for a diffraction pattern is highlighted by a white circle. b) Diffraction pattern of the fault-filling material exhibiting few large and several weak diffraction spots and a diffuse halo. c and d) FIB section 2 cut across the damage-zone garnet next to the narrow fault. c) In STEM mode the damage-zone garnet appears to be completely shattered into pieces <1 µm. The white rectangle marks the position of Fig. 6a and the white circle shows the location of the diffraction pattern. d) Diffraction pattern of the shattered damage-zone garnet. Many weak diffraction spots indicate the presence of numerous small crystals. There is also a diffuse halo in the center of the diffraction pattern. e and f) FIB section 3 cut across the relatively intact host-rock garnet located at ~0.5 µm from a fault. e) The nanostructure of the host-rock garnet reveals features that resemble subgrains. The white circle highlights the location chosen for a diffraction pattern. f) The diffraction pattern of the area shown in e) presents a crystalline structure.

formation of subgrains with diameters of ~ 0.5 to 2 µm (Fig. 5e, f).

The experimental micro- and nanostructures of the damage-zone garnet are strikingly similar to what Austrheim et al. (2017) described as "pulverization structures" in a garnet cut by a pseudotachylyte-vein presumably produced during coseismic faulting of granulites from the Bergen Arcs, Norway, and to those found in garnets from mylonitic micaschists in the Sesia Zone, Swiss Alps (Trepmann and Stöckhert, 2002). One characteristic feature of pulverization structures is the absence or the low amount of shearing of the fragments (Austrheim et al., 2017; Rempe et al., 2013). For our sample, it was not possible to evaluate the extent of shearing of the fragments of the damage-zone garnet by measuring their relative orientations using electron-backscatter diffraction, because most of them are less than 50 nm in diameter (Fig. 6). Taking the acoustic emissions as indicator, faulting and associated pulverization of the wall rock occurred at ~10 to 19 % axial strain (Fig. 2), i.e., only about half the total axial strain of ~40 %. Thus, it is likely that the fragmented garnet experienced some shearing during further deformation as evidenced by the 'tailing' of the damage-zone garnet into the fault (red arrow in Fig. 3d). Though, we can exclude significant shearing, because the fragments' arrangement still mimics a typical garnet-crystal shape (Figs. 3c, 4a, 5c). Straining after pulverization was most likely accommodated by lawsonite dehydration, monitored in-situ during deformation (Incel et al., 2017), involving a solid volume change of around −20 %.

Observed wall-rock damage of rocks from upper crustal depth (<15 km) has been explained by high strain rates and stresses around a dynamically propagating rupture tip (Aben et al., 2016; Bhat et al., 2012; Doan and Gary, 2009; Dor et al., 2006; Griffith et al., 2018; Mitchell et al., 2011; Reches and Dewers, 2005; Rempe et al., 2013; Xu and Ben-Zion, 2017). Recently published studies highlight the role of dilation for the pulverization of rocks during seismic events (Xu and Ben-Zion, 2017; Griffith et al., 2018). In the context of shock-loading, Grady (1982) modeled the inertial or kinetic energy necessary to create new fracture surfaces. Later, Glenn and Chudnovsky (1986) extended this model by accounting for the strain energy stored in the solid before its tensile strength is reached. Based on the extended model, fragment size will not vary over a wide range of strain rates (strain-energy-dominated regime) until kinetic energy dominates over strain energy (kinetic-energy-dominated regime) when fragment size exponentially decays with increasing strain rate. This leads Griffith et al. (2018) to infer that fragment size in pulverized damage zones potentially correlates with strain rate only within close distance (few centimeters) to the fault for natural systems where the highest strain rates

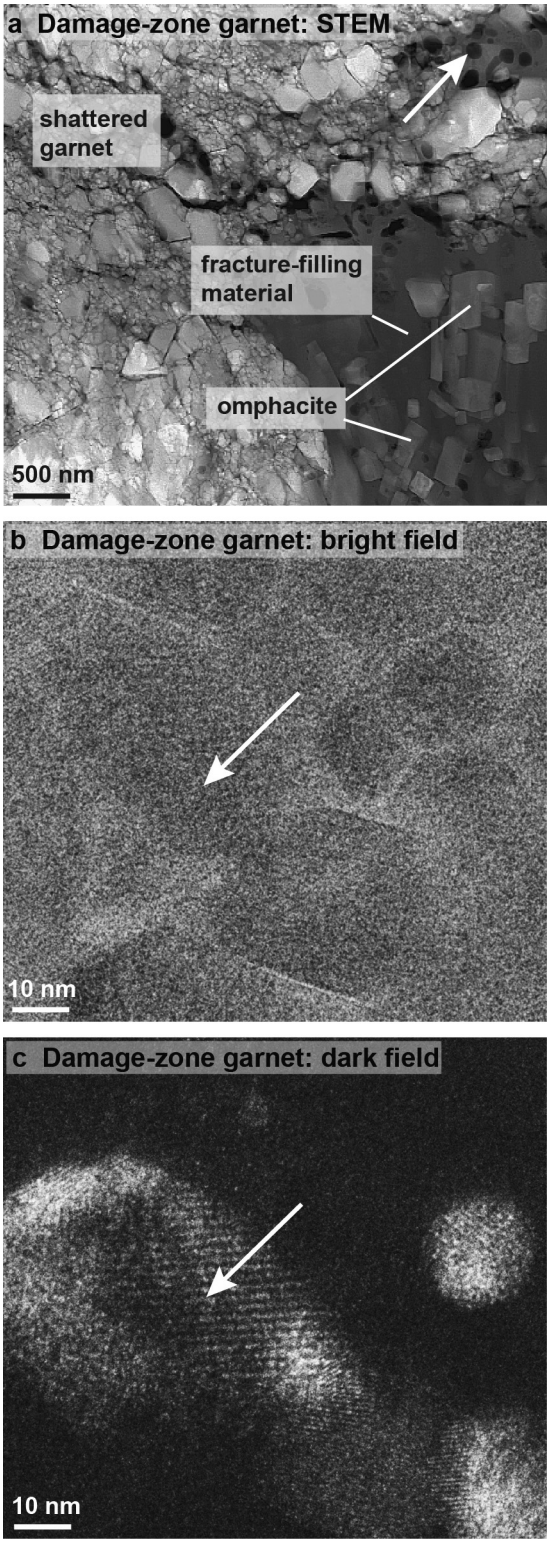

Fig. 6. Transmission electron microscopy images of the shattered damage-zone garnet. a) STEM image revealing the fault-filling material surrounding the damage-zone garnet. Within this material vesicles (white arrow) and idiomorphic omphacite crystals can be found. b) Bright-field image taken in the same zone as the diffraction pattern (Fig. 5c, d). c) The same area as shown in b) taken in dark-field mode. The large grain marked by the white arrow shows subdomains (≤10 nm) that are slightly tilted.

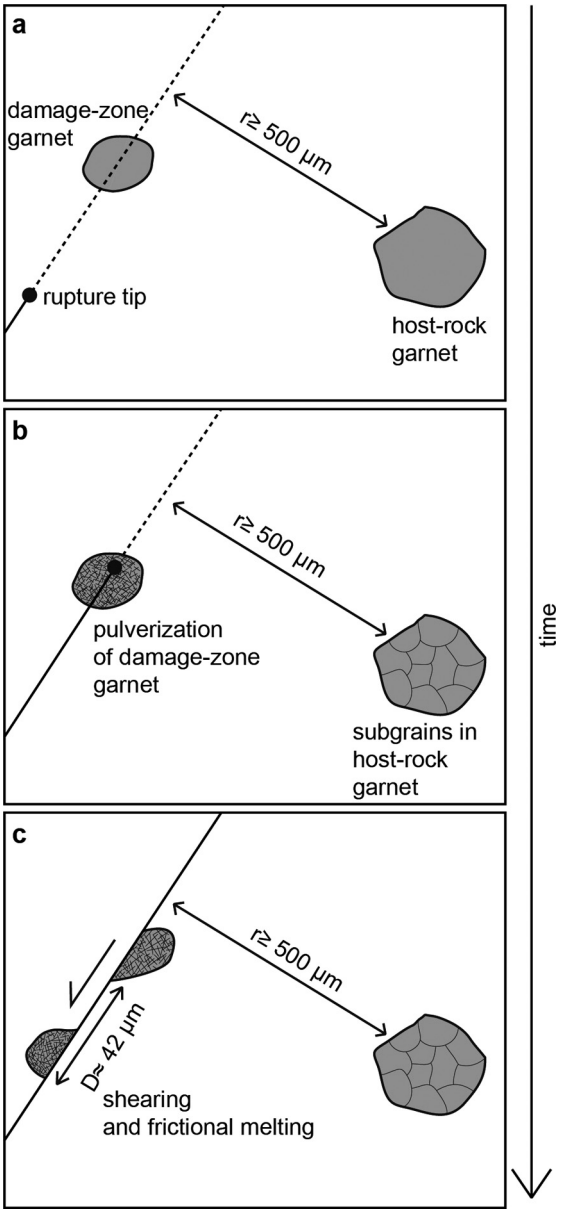

Fig. 7. a) Prior to rupture, both garnet crystals are intact. b) The rupture tip passes through the damage-zone garnet that shows pulverization with fragment sizes ranging between 10 to 500 nm. The host-rock garnet is located at around 500 µm from the nearest fault and shows the formation of subgrains. c) Shearing behind the rupture tip causes the displacement of the garnet halves and eventually frictional melting of the fault surfaces.

are expected. Here, we test whether stress and strain rate fields associated with a dynamically propagating mode II crack tip, are in agreement with the two different nanostructures of the damage-zone garnet showing extensive fragmentation and the host-rock garnet exhibiting subgrain formation (Fig. 7a, b). We rely on linear elastic fracture mechanics (Freund, 1990) to calculate the peak tensile stress as well as the peak strain rate with increasing distance from the fault plane. For the calculations, we used a density $\rho = 3{,}000\ \mathrm{kg\,m^{-3}}$, a shear modulus $\mu = 64$ GPa for glaucophane (Bezacier et al., 2010), a Poisson's ratio $\upsilon = 0.22$ (Cao et al., 2013), and two different rupture velocities $v_r = 0.8c_s$ and $v_r = 0.9c_s$ with the shear wave velocity $c_s = 4618\ \mathrm{m\,s^{-1}}$. We used two different garnet tensile strengths σ_* of 433 MPa ($\sigma_{*\,\mathrm{min}}$; Kavner, 2007) and 4.3 GPa ($\sigma_{*\,\mathrm{max}}$; Pardavi-Horváth, 1984) deduced using reported compressive strengths of either garnet aggregates or garnet single crystals assuming that the tensile strength of a solid is around a third of its compressive strength (Hobbs, 1964). The microstructural observations indicate a co-seismic slip of a few tens

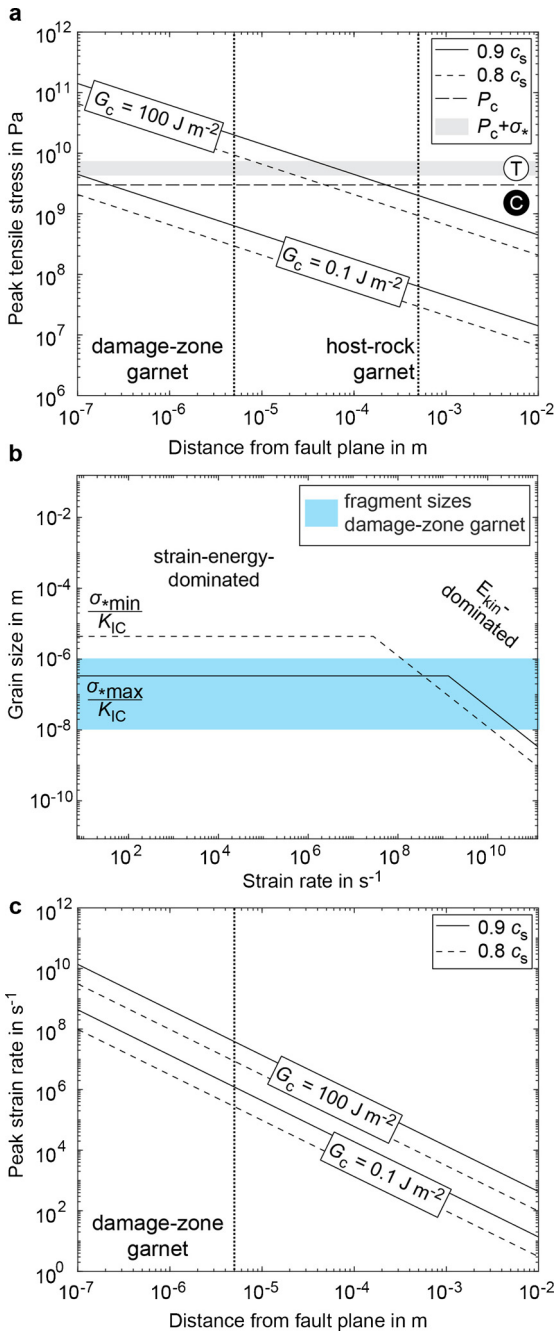

Fig. 8. a) Peak tensile stress over distance from the fault plane for two different rupture speeds v_r ($0.8c_s$ and $0.9c_s$) and two different fracture energies G_c (0.1 J m^{-2} and 100 J m^{-2}; Passelègue et al., 2016). Garnet's tensile strength (grey area) is only exceeded close to the fault at the position of the damage-zone garnet assuming high fracture energies. b) Grain size versus strain rate plot based on the models of Grady (1982) and Glenn and Chudnovsky (1986). Consistency between the calculation and the measured fragment size (~10 nm to 1 μm) is only reached for high garnet tensile strengths of 4.3 GPa (Pardavi-Horváth, 1984). c) Peak strain rates as a function of distance from the fault plane. T = tension; C = compression; P_c = confining pressure; $P_c + \sigma_*$ = range in tensile strength of garnet (Kavner, 2007; Pardavi-Horváth, 1984); σ_* = tensile strength; $\sigma_{*\,min} = 433$ MPa (Kavner, 2007); $\sigma_{*\,max} = 4.3$ GPa (Pardavi-Horváth, 1984); c_s = shear wave velocity; K_{IC} = fracture toughness (here: ~1.5 MPa m$^{1/2}$; Mezeix and Green, 2006).

of micrometers (Figs. 3c; 4a) corresponding to a range in fracture energy G_c of ~0.1 to 100 J m^{-2} (Passelègue et al., 2016). Independent of the value of G_c, the calculated peak tensile stresses do not exceed garnet's tensile strength at the position of the host-rock garnet (Fig. 8a) in accord with the nanostructural observation that the host-rock garnet mostly shows features resembling subgrains (Figs. 5e). On the contrary, assuming high fracture energies, the calculated peak-tensile stress exceeds garnet's tensile strength within the entire damage-zone garnet (Fig. 8a). The result that the damage-zone garnet experienced a peak tensile stress beyond garnet's tensile strength correlates well with our nanostructural observations revealing numerous nanometer-sized fragments (Figs. 5c; 6a). To test whether pulverization of the damage-zone garnet is dominated by either strain energy or kinetic energy, we followed a similar approach as presented in Griffith et al. (2018) to predict the fragment diameter d as a function of strain rate $\dot{\varepsilon}$ using

$$d = 4\left(\frac{\alpha}{3}\right)^{1/2} \sinh\left(\frac{\phi}{3}\right) \tag{1}$$

where

$$\phi = \sinh^{-1}\beta\left(\frac{3}{\alpha}\right)^{\frac{3}{2}}, \tag{2}$$

$$\alpha = \frac{2\beta}{R} + \frac{5}{3}\left(\frac{\sigma_*}{\rho c_p \dot{\varepsilon}}\right)^2, \tag{3}$$

and

$$\beta = \frac{5}{2}\left(\frac{K_{IC}}{\rho c \dot{\varepsilon}}\right)^2. \tag{4}$$

For the calculation we used an initial damage-zone-garnet radius $R = 5$ μm, a garnet (almandine) density $\rho_{Grt} = 4324$ kg m^{-3} (Hacker et al., 2003), a compression wave speed $c = 7132$ m s^{-1}, and a garnet fracture toughness $K_{IC} = 1.5$ MPa m$^{1/2}$ (Mezeix and Green, 2006). Assuming strain values of less than one and a passing-by time of a dynamic rupture in the order of 10^{-6} s results in strain rates $<10^6$ s^{-1}. At these deformation rates, consistency between our calculation and the measured fragment size (blue area in Fig. 8b) is only reached by taking a high garnet tensile strength reported from single crystal experiments (Pardavi-Horváth, 1984) revealing that fragmentation is more likely to be dominated by strain-energy (Fig. 8b). Griffith et al. (2018) observed fragmentation at strain rates of 10^0 to 10^2 s^{-1}. Such strain rates ranging between 10^0 and 10^6 s^{-1} are realized at the position of the damage-zone garnet (Fig. 8c). Linear elastic fracture mechanics provides an asymptotic solution for a semi-infinite crack that is only valid in the near-tip field (Freund, 1990) requiring the length of the crack to be much longer than the width of the investigated crack-tip zone. Our sample is only a few millimeters in size hence this requirement is difficult to satisfy, because of the little length difference between the maximum shear-fracture length of ~3 mm relative to the distance of the host-rock garnets to the shear fracture (~0.5 to 1.5 mm).

Our experimental observations of extensively damaged garnets only in close vicinity to the fault are in accord with a recently published theoretical study revealing that the width of the damage-zone decreases while the extent in off-fault damage increases with depth (Okubo et al., 2019). Consequently, the off-fault damage will be confined to a narrow zone around the fault at deeper depth.

4.2. Frictional melting of blueschist

Sliding of the fracture surfaces in mode II causes a temperature increase, which may eventually lead to melting of the fracture surfaces (Fig. 7c). We deduce the presence of a solidified melt from the amorphous material present in the fault-filling material (Fig. 5a, b) that in some places intruded into the shattered

damage-zone garnet (Fig. 6a). In this "melting scenario", the vesicles in the amorphous material are interpreted to reflect fluid exsolution during decompression of the melt and the observed idiomorphic omphacite crystals to have nucleated and grown during cooling of the melt (Fig. 6a). Assuming a wet basalt solidus temperature T_s of ~1,000 K at ~3 GPa (Hacker et al., 2003), a sliding-related increase in temperature of 280–360 K over the temperatures prevailing during the AE activity (640–720 K) suffice to cause local melting. After Cardwell et al. (1978), the temperature rise ΔT on a slipping fault can be expressed as

$$\Delta T = \frac{\tau D}{\rho c_p \sqrt{\pi \kappa t_{\text{slip}}}} \tag{5}$$

with shear stress τ, shear displacement D, density ρ, specific heat capacity c_p (1,100 $\text{J kg}^{-1}\text{K}^{-1}$ at ~1,000 K; Hartlieb et al., 2016), thermal diffusivity κ ($\sim 10^{-6}$ $\text{m}^2\,\text{s}^{-1}$), and slip duration t_{slip}. The nominal shear stress τ and normal stress σ_n acting on the fault are ~1.25 GPa and 4.25 GPa, respectively (with $\theta \approx 45°$, $\sigma_1 = 5.5$ GPa, and $\sigma_3 = 3$ GPa). Assuming a minimum total displacement $D = 42$ µm (Figs. 3c) and only 10 % of that slip to have happened co-seismically and a sliding velocity of ~1 m s^{-1} (for a crack-like rupture; Schubnel et al., 2013) gives a slip duration $t_{\text{slip}} \sim 4.2 \times 10^{-6}$ s. These estimates result in a ΔT of >390 K indeed exceeding the difference between prevailing assembly temperature and the expected sample's solidus temperature.

The presence of a melt film on the fault surfaces may lead to weakening due to fault lubrication allowing unstable slip (Di Toro et al., 2006). Dynamic shear strength τ_f of a fault with a continuous melt film depends linearly on the ratio between the width w of the molten zone and the slip displacement (e.g., Ferrand et al., 2018)

$$\tau_f = \frac{\rho(Hc_p\Delta T)}{(1-\eta)}\frac{w}{D} \tag{6}$$

with the latent heat of fusion H ($\approx 3 \times 10^5$ J kg^{-1}) and the radiation efficiency η. In our sample, the narrow fault that contains molten material shows a width of $w \approx$ 100–500 nm. Previous studies showed that the seismic efficiency ranges between $0.1 < \eta < 0.5$ (Poli and Prieto, 2016). Within this span, equation (2) gives a dynamic shear strength of the fault as low as ~7 to 66 MPa (Fig. 9a) corresponding to friction coefficients of ~0.002 to 0.015 (Fig. 9b), i.e. significant lubrication.

5. Conclusion and implications

We investigated two garnet crystals within a lawsonite-blueschist sample that are located at different distances to the nearest fault created during brittle failure at ultra-high-pressure conditions. The micro- and nanostructures observed in the damage-zone garnet, which resemble pulverization structures in natural rocks inherited at upper as well as at lower crustal depths, can be explained by extensive fragmentation due to high tensile stresses and strain rates associated with a dynamically propagating shear fracture. After the passage of the crack tip, frictional sliding of the fault surfaces causes melting and fault lubrication. Our experimental study emphasizes the importance of dynamic rupture as a brittle precursor to unstable frictional slip even at upper mantle depths.

Acknowledgements

The authors thank the two reviewers Greg Hirth and Ashley Griffith for their comments that helped improving the manuscript.

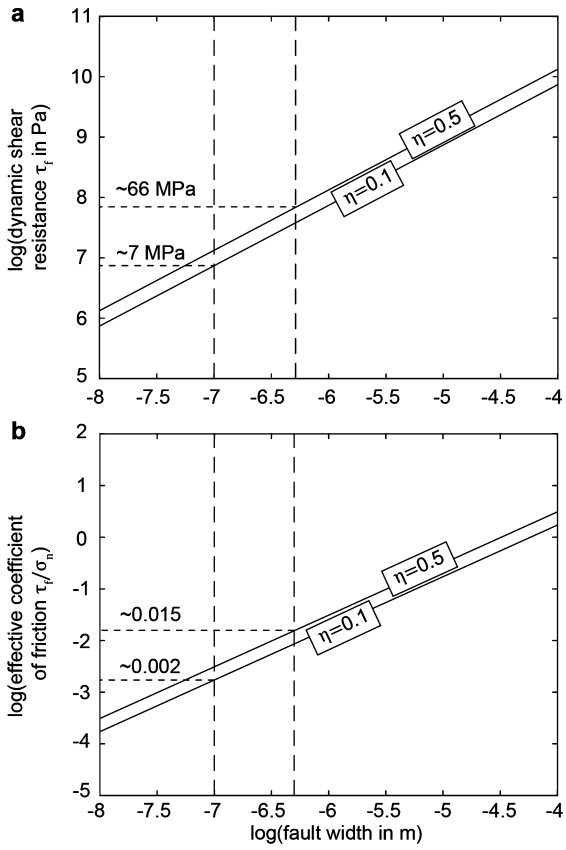

Fig. 9. a) Dynamic shear resistance and b) effective coefficient of friction versus width of the slip-associated melt layer. The vertical dashed lines mark the measured width of the molten zone filling out the fault along which a garnet pair is dissected and displaced (Fig. 3c). Recent studies show that the radiative efficiency increases with depth ranging between $\eta = 0.1$ to 0.5 for intermediate depth earthquakes (50–300 km). The dashed horizontal lines indicate the intercept of this radiative efficiency range and the width range of the molten zone (~100 to 500 nm) measured in the sample. The dynamic shear resistance would be ~7 to 66 MPa (a) resulting in an effective coefficient of friction of ~0.002 to 0.015 (b).

The authors also thank Anja Schreiber for the preparation of the FIB sections, Damien Deldicque for his help at the SEM and the TEM, and Christian Chopin who provided the blueschist sample. Special thanks go to Frans Aben, François Passelègue, and Yehuda Ben-Zion for their help and their time for discussions and to Paul Meakin for a careful review of an early version of the manuscript. The study was realized partly thanks to funding from the Alexander von Humboldt-Foundation (Feodor Lynen-fellowship to S.I.) and support from Geo.X in form of a travel Grant (to S.I.). Further funding came from the People Program (Marie Curie Actions) of the European Union's Seventh Framework Programme FP7/2017-2013/ and Horizon 2020 under REA grant agreements n° 604713 (to A.S.) and n° 669972 (to B.J.), EAR-1661489 for the development of AE experiments (Y.W.). This research used resources of the Advanced Photon Source, a U.S. Department of Energy Office of Science User Facility operated by Argonne National Laboratory (contract n° DE-AC02-06CH11357). Financial support (for H.F) through funding provided by the German Helmholtz Recruiting Initiative (award number I-044-16-01) to Liane G. Benning from the GFZ is acknowledged.

References

Aben, F.M., Doan, M., Mitchell, T.M., Toussaint, R., Reuschlé, T., Fondriest, M., Gratier, J., Renard, F., 2016. Dynamic fracturing by successive coseismic loadings leads to pulverization in active fault zones. J. Geophys. Res., Solid Earth 121, 2338–2360. https://doi.org/10.1002/2015JB012542.

Angiboust, S., Agard, P., Yamato, P., Raimbourg, H., 2012. Eclogite breccias in a subducted ophiolite: a record of intermediatedepth earthquakes? Geology 40, 707–710. https://doi.org/10.1130/G32925.1.

Austrheim, H., Dunkel, K.G., Plümper, O., Ildefonse, B., Liu, Y., Jamtveit, B., 2017. Fragmentation of wall rock garnets during deep crustal earthquakes. Sci. Adv. 3, 1–7. https://doi.org/10.1126/sciadv.1602067.

Ben-Zion, Y., 2003. Appendix 2, Key formulas in earthquake seismology. In: Int. Handb. Earthq. Eng. Seismol. Part B, pp. 1857–1875.

Bezacier, L., Reynard, B., Bass, J.D., Wang, J., Mainprice, D., 2010. Elasticity of glaucophane, seismic velocities and anisotropy of the subducted oceanic crust. Tectonophysics 494, 201–210. https://doi.org/10.1016/j.tecto.2010.09.011.

Bhat, H.S., Rosakis, A.J., Sammis, C.G., 2012. A micromechanics based constitutive model for brittle failure at high strain rates. J. Appl. Mech. 79, 31016. https://doi.org/10.1115/1.4005897.

Braeck, S., Podladchikov, Y.Y., 2007. Spontaneous thermal runaway as an ultimate failure mechanism of materials. Phys. Rev. Lett. 98. https://doi.org/10.1103/PhysRevLett.98.095504.

Cao, Y., Jung, H., Song, S., 2013. Petro-fabrics and seismic properties of blueschist and eclogite in the North Qilian suture zone, NW China: implications for the low-velocity upper layer in subducting slab, trench-parallel seismic anisotropy, and eclogite detectability in the subduction zone. J. Geophys. Res., Solid Earth 118, 3037–3058. https://doi.org/10.1002/jgrb.50212.

Cardwell, R.K., Chinn, D.S., Moore, G.F., Turcotte, D.L., 1978. Frictional heating on a fault zone with finite thickness. Geophys. J. R. Astron. Soc. 52, 525–530. https://doi.org/10.1111/j.1365-246X.1978.tb04247.x.

Di Toro, G., Hirose, T., Nielsen, S., Pennacchioni, G., Shimamoto, T., 2006. Natural and experimental evidence during earthquakes. Science 80 (311), 647–649. https://doi.org/10.1126/science.1121012.

Doan, M.L., Gary, G., 2009. Rock pulverization at high strain rate near the SanAndreas fault. Nat. Geosci. 2, 709–712. https://doi.org/10.1038/ngeo640.

Dor, O., Ben-Zion, Y., Rockwell, T.K., Brune, J., 2006. Pulverized rocks in the Mojave section of the San Andreas Fault Zone. Earth Planet. Sci. Lett. 245, 642–654. https://doi.org/10.1016/j.epsl.2006.03.034.

Ferrand, T.P., Hilairet, N., Incel, S., Deldicque, D., Labrousse, L., Gasc, J., Renner, J., Wang, Y., Green, H.W., Schubnel, A., 2017. Dehydration-driven stress transfer triggers intermediate-depth earthquakes. Nat. Commun. 8, 1–11. https://doi.org/10.1038/ncomms15247.

Ferrand, T.P., Labrousse, L., Eloy, G., Fabbri, O., Hilairet, N., Schubnel, A., 2018. Energy balance from a mantle pseudotachylyte, Balmuccia, Italy. J. Geophys. Res., Solid Earth. https://doi.org/10.1002/2017JB014795.

Freund, L.B., 1990. Dynamic Fracture Mechanics. Cambridge University Press.

Gasc, J., Hilairet, N., Yu, T., Ferrand, T., Schubnel, A., Wang, Y., 2017. Faulting of natural serpentinite: implications for intermediate-depth seismicity. Earth Planet. Sci. Lett. 474, 138–147. https://doi.org/10.1016/j.epsl.2017.06.016.

Gasc, J., Schubnel, A., Brunet, F., Guillon, S., Mueller, H.J., Lathe, C., 2011. Simultaneous acoustic emissions monitoring and synchrotron X-ray diffraction at high pressure and temperature: calibration and application to serpentinite dehydration. Phys. Earth Planet. Inter. 189, 121–133. https://doi.org/10.1016/j.pepi.2011.08.003.

Glenn, L.A., Chudnovsky, A., 1986. Strain-energy effects on dynamic fragmentation. J. Appl. Phys. 59, 1379–1380.

Grady, D.E., 1982. Local inertial effects in dynamic fragmentation. J. Appl. Phys. 53, 322–325. https://doi.org/10.1063/1.329934.

Green II, H.W., Burnley, P.C., 1989. A new self-organizing mechanism for deep-focus earthquakes. Nature 341, 733–737. https://doi.org/10.1038/341733a0.

Griffith, W.A., St. Julien, R.C., Ghaffari, H.O., Barber, T.J., 2018. A tensile origin for fault rock pulverization. J. Geophys. Res., Solid Earth 123, 7055–7073. https://doi.org/10.1029/2018JB015786.

Guermani, A., Pennacchioni, G., 1998. Brittle precursors of plastic deformation in a granite: an example from the Mont Blanc massif (Helvetic, western Alps). J. Struct. Geol. 20, 135–148. https://doi.org/10.1016/S0191-8141(97)00080-1.

Hacker, B.R., Abers, G.A., Peacock, S.M., 2003. Subduction factory 1. Theoretical mineralogy, densities, seismic wave speeds, and H_2O contents. J. Geophys. Res., Solid Earth 108, 1–26. https://doi.org/10.1029/2001JB001127.

Hartlieb, P., Toifl, M., Kuchar, F., Meisels, R., Antretter, T., 2016. Thermo-physical properties of selected hard rocks and their relation to microwave-assisted comminution. Miner. Eng. 91, 34–41. https://doi.org/10.1016/j.mineng.2015.11.008.

Hobbs, D.W., 1964. The tensile strength of rocks. Int. J. Rock Mech. Min. Sci. Geomech. Abstr. I, 385–396.

Incel, S., Hilairet, N., Labrousse, L., John, T., Deldicque, D., Ferrand, T.P., Wang, Y., Morales, L., Schubnel, A., 2017. Laboratory earthquakes triggered during eclogitization of lawsonite-bearing blueschist. Earth Planet. Sci. Lett. 459, 320–331. https://doi.org/10.1016/j.epsl.2016.11.047.

Incel, S., Labrousse, L., Hilairet, N., John, T., Gasc, J., Shi, F., Wang, Y., Andersen, T.B., Renard, F., Jamtveit, B., Schubnel, A., 2019. Reaction-induced embrittlement of the lower continental crust. Geology 47, 235–238. https://doi.org/10.1130/G45527.1.

Jamtveit, B., Petley-Ragan, A., Incel, S., Dunkel, K.G., Aupart, C., Austrheim, H., Corfu, F., Menegon, L., Renard, F., 2019. The effects of earthquakes and fluids on the metamorphism of the lower continental crust. J. Geophys. Res., Solid Earth. https://doi.org/10.1029/2018JB016461.

John, T., Medvedev, S., Rüpke, L.H., Andersen, T.B., Podladchikov, Y.Y., Austrheim, H., 2009. Generation of intermediate-depth earthquakes by self-localizing thermal runaway. Nat. Geosci. 2, 137–140. https://doi.org/10.1038/ngeo419.

Kavner, A., 2007. Garnet yield strength at high pressures and implications for upper mantle and transition zone rheology. J. Geophys. Res., Solid Earth 112, 1–9. https://doi.org/10.1029/2007JB004931.

Kelemen, P.B., Hirth, G., 2007. A periodic shear-heating mechanism for intermediate-depth earthquakes in the mantle. Nature 446, 787–790. https://doi.org/10.1038/nature05717.

Kirby, S.H., 1987. Localized polymorphic phase transformations in high-pressure faults and applications to the physical mechanism of deep earthquakes. J. Geophys. Res., Solid Earth 92, 13789–13800. https://doi.org/10.1029/JB092iB13p13789.

Kirkpatrick, J.D., Rowe, C.D., 2013. Disappearing ink: how pseudotachylytes are lost from the rock record. J. Struct. Geol. 52, 183–198. https://doi.org/10.1016/j.jsg.2013.03.003.

Mancktelow, N.S., 2006. How ductile are ductile shear zones? Geology 34, 345–348. https://doi.org/10.1130/G22260.1.

McKenzie, D., Brune, J.N., 1972. Melting on fault planes during large earthquakes. Geophys. J. R. Astron. Soc. 29, 65–78. https://doi.org/10.1111/j.1365-246X.1972.tb06152.x.

Mezeix, L., Green, D.J., 2006. Comparison of the mechanical properties of single crystal and polycrystalline yttrium aluminum garnet. Int. J. Appl. Ceram. Technol. 3, 166–176. https://doi.org/10.1111/j.1744-7402.2006.02068.x.

Mitchell, T.M., Ben-Zion, Y., Shimamoto, T., 2011. Pulverized fault rocks and damage asymmetry along the Arima-Takatsuki Tectonic Line, Japan. Earth Planet. Sci. Lett. 308, 284–297. https://doi.org/10.1016/j.epsl.2011.04.023.

Mitchell, T.M., Faulkner, D.R., 2009. The nature and origin of off-fault damage surrounding strike-slip fault zones with a wide range of displacements: a field study from the Atacama fault system, northern Chile. J. Struct. Geol. 31, 802–816. https://doi.org/10.1016/j.jsg.2009.05.002.

Okazaki, K., Hirth, G., 2016. Dehydration of lawsonite could directly trigger earthquakes in subducting oceanic crust. Nature 530, 81–84. https://doi.org/10.1038/nature16501.

Okubo, K., Bhat, H.S., Rougier, E., Marty, S., Schubnel, A., Lei, Z., Knight, E.E., Klinger, Y., 2019. Dynamics, radiation and overall energy budget of earthquake rupture with coseismic off-fault damage. arXiv:1901.01771.

Pardavi-Horváth, M., 1984. Microhardness and brittle fracture of garnet single crystals. J. Mater. Sci. 19, 1159–1170. https://doi.org/10.1007/BF01120025.

Passelègue, F.X., Schubnel, A., Nielsen, S., Bhat, H.S., Deldicque, D., Madariaga, R., 2016. Dynamic rupture processes inferred from laboratory microearthquakes. J. Geophys. Res., Solid Earth 121, 4343–4365. https://doi.org/10.1002/2015JB012694.

Petley-Ragan, A., Ben-Zion, Y., Austrheim, H., Ildefonse, B., Renard, F., Jamtveit, B., 2019. Dynamic earthquake rupture in the lower crust. Sci. Adv. 5, eaaw0913. https://doi.org/10.1126/sciadv.aaw0913.

Petley-Ragan, A., Dunkel, K.G., Austrheim, H., Ildefonse, B., Jamtveit, B., 2018. Microstructural records of earthquakes in the lower crust and associated fluid-driven metamorphism in plagioclase-rich granulites. J. Geophys. Res., Solid Earth 123, 3729–3746. https://doi.org/10.1029/2017JB015348.

Poli, P., Prieto, G.A., 2016. Global rupture parameters for deep and intermediate-depth earthquakes. J. Geophys. Res., Solid Earth 121, 8871–8887. https://doi.org/10.1002/2016JB013521.

Raleigh, C.B., Paterson, M.S., 1965. Experimental deformation of serpentinite and its tectonic implications. J. Geophys. Res. 70, 3965–3985. https://doi.org/10.1029/JZ070i016p03965.

Reches, Z., Dewers, T.A., 2005. Gouge formation by dynamic pulverization during earthquake rupture. Earth Planet. Sci. Lett. 235, 361–374. https://doi.org/10.1016/j.epsl.2005.04.009.

Rempe, M., Mitchell, T., Renner, J., Nippress, S., Ben-Zion, Y., Rockwell, T., 2013. Damage and seismic velocity structure of pulverized rocks near the San Andreas Fault. J. Geophys. Res., Solid Earth 118, 2813–2831. https://doi.org/10.1002/jgrb.50184.

Schubnel, A., Brunet, F., Hilairet, N., Gasc, J., Wang, Y., Green, H.W., 2013. Deep-focus earthquake analogs recorded at high pressure and temperature in the laboratory. Science 80 (341), 1377–1380. https://doi.org/10.1126/science.1240206.

Sibson, R.H., 1975. Generation of pseudotachylyte by ancient seismic faulting. Geophys. J. R. Astron. Soc. 43, 775–794. https://doi.org/10.1111/j.1365-246X.1975.tb06195.x.

Thielmann, M., Rozel, A., Kaus, B.J.P., Ricard, Y., 2015. Intermediate-depth earthquake generation and shear zone formation caused by grain size reduction and shear heating. Geology 43, 791–794. https://doi.org/10.1130/G36864.1.

Trepmann, C.A., Stöckhert, B., 2002. Cataclastic deformation of garnet: a record of synseismic loading and postseismic creep. J. Struct. Geol. 24, 1845–1856. https://doi.org/10.1016/S0191-8141(02)00004-4.

Wang, Y., Durham, W.B., Getting, I.C., Weidner, D.J., 2003. The deformation-DIA: a new apparatus for high temperature triaxial deformation to pres-

sures up to 15 GPa. Rev. Sci. Instrum. 74, 3002–3011. https://doi.org/10.1063/1.1570948.

Xu, S., Ben-Zion, Y., 2017. Theoretical constraints on dynamic pulverization of fault zone rocks. Geophys. J. Int. 209, 282–296. https://doi.org/10.1093/gji/ggx033.

Yund, R.A., Blanpied, M.L., Tullis, T.E., Weeks, J.D., 1990. Amorphous material in high strain experimental fault gouges. J. Geophys. Res. 95, 15,589–15,602.